

Chapter 4

Results

In this chapter the results obtained from isotopic studies of eleven coarse-grained Ca-Al-Rich inclusions from Efremovka and Grosnaja meteorites by the ion microprobe are presented. Magnesium, potassium and calcium isotopic studies were carried out on these CAIs using the techniques and procedures described in Chapter 2. Mg-Al isotopic studies were carried out on all the CAIs [E2 and E59 (type A); E36 and E60 (type B2); E40, E44 and E65 (type B1); E50 (hibonite-rich); GR2 (type C); GR4 (type A); and GR7 (type B)]. The CAIs E44, E50 and E65 were analyzed for their potassium and calcium isotopic compositions.

4.1 Results from Mg-Al Isotopic Studies

Mg-Al isotopic studies were carried out to determine intrinsic Mg isotopic mass fractionation $F(\text{Mg})$ (Eq.2.2, Chapter 2) for the Efremovka CAIs, and non linear $\delta^{26}\text{Mg}$ excess (Eq.2.6, Chapter 2) and $^{27}\text{Al}/^{24}\text{Mg}$ values in all the CAIs.

The $F(\text{Mg})$ values were determined for the two major magnesium bearing phases, melilite and spinel, present in the peripheral and interior regions of several of the Efremovka CAIs. The measurements were carried out in a continuous run for individual CAI, and terrestrial standards were measured at regular intervals. Only in the case of E2 spinels in the rim were also analyzed. Further, a systematic study of spatial variation of $F(\text{Mg})$ within the CAIs were carried out in the case of E2 and E40. The results obtained from these

analyses are presented in Tables 4.1-4.4. The errors in $F(\text{Mg})$ values have been computed by taking into account the measurement uncertainties in $\Delta^{25}\text{Mg}$ for both the meteoritic phases and terrestrial standards. The $F(\text{Mg})$ values of spinels in some CAIs are slightly higher than melilite, however, it is not significant in view of the measurement uncertainties of $\sim 1.5\text{‰}/\text{amu}(2\sigma_m)$. This difference could partly be due to the fact that the terrestrial melilite standard used by us has a high Akermanite content [$\sim 65\text{ mole\%}$] compared to meteoritic melilite that spans a wide range of composition [$\sim 10\text{-}70\text{ mole\%}$].

The results (Tables 4.1 and 4.2) suggest significant differences in $F(\text{Mg})$ values between the peripheral and interior regions of the CAIs E2 and E40, and non-systematic spatial variation in $F(\text{Mg})$ values in E50. A detailed study was therefore carried out to determine the spatial variation in $F(\text{Mg})$ values for both melilite and spinel phases in E2 and E40 (Tables 4.3-4.4). In the case of E40 the studies were carried out along two nearly radial traverses one of which was close to an electron probe traverse that provided data on melilite composition. The melilite composition in E2 and E40 show similar trends with the near rim melilite being gehlenitic (more refractory, high Al/Mg) while melilite in the interior are akermanitic (less refractory, low Al/Mg). However, the $F(\text{Mg})$ values for melilite in these two CAIs show opposite trend. Melilite in the near rim region in E2 is enriched in the lighter isotopes [$F(\text{Mg}) \leq 0$] and those in the interior are enriched in the heavy isotopes; in E40 the trend is reverse with melilite in the near rim region enriched in the heavy isotopes and those in the interior have near normal Mg isotopic composition. Additionally, the $F(\text{Mg})$ values for all spinels in E40 do not match the melilite data. Some of the spinel grains near the rim and in the interior have higher $F(\text{Mg})$ values compared to those of melilite, much outside the limits of experimental uncertainties.

The magnesium isotopic mass fractionation in the CAI E2 was measured earlier by Fahey et al. (1987b). Even though the fractionation trend observed by us in this is similar to that reported by Fahey et al. (1987b), there are some differences in the absolute values. We obtain systematically lower $F(\text{Mg})$ values for the near-rim phases than Fahey et al. (1987b). Since the measurements were carried out on two different sections of E2, which is the largest

CAI in Efremovka measuring couple of cms across, these differences could be in part due to spatial dependence of the intensity of the process responsible for producing the observed intrinsic fractionation in this CAI. The data for the phases in the interior of this CAI showed a spread in F(Mg) values which agree with the range of values (7 to 11%) reported by Fahey et al. (1987b). We shall now consider the data pertaining to non-linear excess in ^{26}Mg in the CAIs from the Efremovka and Grosnaja meteorites.

If non-linear excess in ^{26}Mg ($\delta^{26}\text{Mg} > 0$, Eq.2.6, Chapter 2) is present in meteoritic phases, and if such an excess is of radiogenic origin, caused by the decay of the short-lived radionuclide ^{26}Al ($t_{1/2} \sim 0.7\text{Ma}$), the measured ^{26}Mg has two components and one can write :

$$\begin{aligned} \left(\frac{^{26}\text{Mg}}{^{24}\text{Mg}}\right)_m &= \left(\frac{^{26}\text{Mg}}{^{24}\text{Mg}}\right)_i + \left(\frac{^{26}\text{Mg}^*}{^{24}\text{Mg}}\right) \\ &= \left(\frac{^{26}\text{Mg}}{^{24}\text{Mg}}\right)_i + \left(\frac{^{26}\text{Al}}{^{27}\text{Al}}\right)_i \left(\frac{^{27}\text{Al}}{^{24}\text{Mg}}\right)_m \end{aligned} \quad (4.1)$$

where m stands for the measured isotopic ratio, i for the initial ratio at the time of formation of meteoritic phases (e.g. CAIs) and "*" represents the radiogenic component. If a CAI has different mineral phases with varying $^{27}\text{Al}/^{24}\text{Mg}$ values then Eq. 4.1 describes the evolution of the Mg-Al isotopic system. The intercept and slope of the best-fit line represent the initial $^{26}\text{Mg}/^{24}\text{Mg}$ and $^{26}\text{Al}/^{27}\text{Al}$ at the time of closure of the Mg-Al isotope system in the CAI. The procedure for obtaining a best-fit line to a set of data with errors in both coordinates have been given by York (1967, 1969), Williamson (1968) and Provost (1990). The intercept and slope of the Mg-Al evolution diagrams for different CAIs analyzed by us were determined by using the programs developed by Lugmair (1991) and Provost (1990). It should be noted here that secondary processes affecting the CAIs can lead to possible exchange of Mg between different phases within the CAI or between CAI and external phases/reservoir that can disturb the Mg-Al isotopic system and result in deviations from the above relation.

The fractionation corrected ^{26}Mg excess ($\delta^{26}\text{Mg}$) and the $^{27}\text{Al}/^{24}\text{Mg}$ values were

measured in all the Efremovka and Grosnaja CAIs, and the results are given in Tables 4.1-4.5. The $^{27}\text{Al}/^{24}\text{Mg}$ values were determined from the $^{27}\text{Al}^+ / ^{24}\text{Mg}^+$ values measured using the ion microprobe, and the Mg-Al yield factors [Table 2.2, Eq.2.7, Chapter2]. The different phases that have been analyzed are spinel, melilite, pyroxene, and anorthite. Hibonite was also analyzed in the case of E50. The $^{27}\text{Al}/^{24}\text{Mg}$ shows a wide variation in the analyzed phases, spinels and pyroxenes have the lowest values (≤ 3); melilites have intermediate values (1 to 50); and anorthites have the highest values (100 to 1000). The spread in the $^{27}\text{Al}/^{24}\text{Mg}$ values allow us to constrain the slope and the intercept of the Mg-Al evolution diagram for the different CAIs and obtain accurate values for initial magnesium and aluminum isotopic composition at the time of formation of CAIs. In the case of Grosnaja CAIs and some of the Efremovka CAIs (E36, E44, E59, E60 and E65) results pertaining to $\delta^{26}\text{Mg}$ and $^{27}\text{Al}/^{24}\text{Mg}$ values are only given as the measurements were made without the added precaution needed to obtain F(Mg) values. The Mg-Al evolution diagrams for the CAIs were obtained by combining the results presented in Tables 4.1-4.5 and these are shown in Figs.4.1a - 4.1k. Seven CAIs from Efremovka, E2 and E59 (type A), E36 and E60 (type B2), E40, and E65 (type B1), E50 (hibonite-rich), have well behaved Mg-Al isotope systematics with initial $^{26}\text{Al}/^{27}\text{Al}$ ranging from $(3.11 \times 10^{-5}$ to $5.64) \times 10^{-5}$. The correlation in case of CAI E36 is not as good and although the data suggest the presence of radiogenic ^{26}Mg with an initial aluminium isotopic ratio close to the values obtained for the other Efremovka CAIs, we cannot completely rule out the possibility of some disturbances in the magnesium isotopic systematics in this CAI. The CAI E60 (type B2) shows an approximately well behaved systematics with an initial ratio of $(3.11 \pm 0.33) \times 10^{-5}$, although individual anorthite data points show a scatter, and yield $^{26}\text{Al}/^{27}\text{Al}$ ranging from $(1.86$ to $3.75) \times 10^{-5}$. The CAI E44 (type B1) shows a clear sign of disturbance in its Mg-Al isotopic systematics with data for melilite and anorthite showing completely different trends. If we consider the melilite and anorthite data separately, and use spinel and pyroxene as common members, they yield initial $^{26}\text{Al}/^{27}\text{Al}$ value of $(6.7 \pm 2.2) \times 10^{-5}$ (melilite) and $(4.6 \pm 1.1) \times 10^{-6}$ (anorthite) respectively. In the case of Grosnaja CAIs only GR2 (type C) yields a well behaved Mg-Al evolution diagram. However, the initial

$^{26}\text{Al}/^{27}\text{Al}$ value $[(3.14 \pm 0.49) \times 10^{-6}]$, is much lower than the values obtained for the Efremovka CAIs. In the case of GR4 (type A) and GR7 (type B), the data suggest extreme disturbance in the Mg-Al systematics and absence of any correlation between ^{26}Mg excess and $^{27}\text{Al}/^{24}\text{Mg}$ values. The initial $^{26}\text{Mg}/^{24}\text{Mg}$ at the time of formation of the CAIs are near normal within experimental uncertainties except in E60 which shows a 2‰ excess in the $^{26}\text{Mg}/^{24}\text{Mg}$ ratio above the solar system reference value.

Table 4.1: Mg-Al Data

Phase	F(Mg) $\pm 2\sigma_m$	$\delta^{26}\text{Mg}$ $\pm 2\sigma_m$	$^{27}\text{Al}/^{24}\text{Mg}$ $\pm 2\sigma_m$
E2(Type A)			
Spinel*	-2.6 ± 1.5	-1.3 ± 2.2	2.6
Spinel†	6.8 ± 1.5	0.4 ± 1.7	2.5
Melilite*	0.1 ± 1.6	8.1 ± 2.2	22.6 ± 0.7
Melilite*	-2.9 ± 1.2	7.4 ± 4.7	25.7 ± 0.3
Melilite†	3.5 ± 1.4	3.5 ± 2.1	8.5 ± 0.9
Melilite†	7.2 ± 1.7	1.5 ± 2.5	7.9
E40(Type B1)			
Spinel*	4.2 ± 1.6	2.4 ± 2.1	2.6
Spinel†	1.9 ± 2.0	-1.0 ± 2.7	2.5
Melilite*	3.3 ± 1.3	6.7 ± 1.6	13.9 ± 0.7
Melilite*	4.8 ± 1.6	5.5 ± 2.6	18.9 ± 0.2
Melilite†	0.3 ± 1.3	1.9 ± 1.7	5.8
E44(Type B1)			
Spinel†	3.2 ± 2.2	3.0 ± 3.4	2.5
Spinel†	3.7 ± 2.1	2.3 ± 3.2	2.5
Melilite†	3.7 ± 1.4	3.2 ± 1.9	3.0
Melilite*	3.8 ± 1.4	3.4 ± 2.2	10.5 ± 0.1
E65(Type B1)			
Spinel	4.7 ± 1.5	2.5 ± 2.0	2.4
Spinel	4.6 ± 1.5	2.4 ± 1.8	2.5
Melilite	2.8 ± 1.3	3.2 ± 2.7	5.8
Melilite	2.7 ± 1.4	2.5 ± 2.9	6.1
E60(Type B2)			
Melilite*	-1.3 ± 1.6	2.0 ± 2.5	1.5
Melilite†	0.5 ± 1.4	-0.1 ± 2.2	0.4
Melilite†	-0.2 ± 1.5	2.8 ± 2.1	1.1
Spinel	1.6 ± 1.4	2.2 ± 1.5	2.5
E36 (Type B2)			
Melilite*	2.6 ± 1.3	3.97 ± 1.92	13.08 ± 0.28
Melilite†	4.7 ± 1.7	3.70 ± 2.34	21.52 ± 0.80
E59 (Type A)			
Melilite*	4.6 ± 1.4	3.75 ± 2.08	16.7 ± 0.2
Melilite†	3.8 ± 0.9	6.57 ± 3.10	15.9 ± 0.2

Note: F(Mg) and $\delta^{26}\text{Mg}$ are in permil/amu and permil
Errors less than 0.1 are not shown

*Near Rim

† Interior

Table 4.2: Mg-Al Data

Zone	F(Mg) $\pm 2\sigma_m$	$\delta^{26}\text{Mg}$ $\pm 2\sigma_m$	$(^{27}\text{Al}/^{24}\text{Mg})$ $\pm 2\sigma_m$
E50(Multizoned Hibonite-Rich)			
Melilite			
Near Rim	2.11 ± 1.73	4.57 ± 2.72	21.37 ± 0.11
Near Rim	-6.61 ± 2.34	19.02 ± 4.42	23.69 ± 0.06
Me + Sp	8.01 ± 1.76	5.37 ± 3.22	19.69 ± 0.11
Interior (Me + Per)	0.97 ± 1.98	12.76 ± 3.98	32.56 ± 3.36
Interior (Me + Per)	5.50 ± 2.45	7.56 ± 4.46	23.86 ± 0.09
Interior (Me + Per)	5.00 ± 2.15	4.58 ± 4.04	18.86 ± 0.15
Interior (Me + Per)	2.26 ± 1.85	11.37 ± 3.38	24.25 ± 0.28
Interior (Me + Per)	0.50 ± 1.84	4.30 ± 2.74	19.62 ± 0.37
Hibonite Rich	3.46 ± 2.70	14.38 ± 4.44	50.60 ± 0.22
Spinel			
Near Rim	1.06 ± 1.59	0.24 ± 2.22	2.59 ± 0.27
Me + Sp	9.20 ± 1.26	1.17 ± 1.67	2.60 ± 0.01
Me + Sp	8.30 ± 1.34	-0.42 ± 1.99	2.62 ± 0.01
Interior (Me + Per)	0.95 ± 1.50	1.41 ± 2.38	2.70 ± 0.03
Hibonite			
Hibonite Rich	-	7.08 ± 2.20	17.94 ± 0.03
Hibonite Rich	-	5.49 ± 2.38	15.16 ± 0.07

Note: F(Mg) and $\delta^{26}\text{Mg}$ are in permil/amu and permil
 Errors less than 0.1 are not shown

Table 4.3: Mg-Al Data

Position*	F(Mg)	$\delta^{26}\text{Mg}$	$^{27}\text{Al}/^{24}\text{Mg}^\dagger$
μm	$\pm 2\sigma_m$	$\pm 2\sigma_m$	$\pm 2\sigma_m$
E2(Type A)[§]			
Melilite Traverse			
20	0.1 ± 1.6	8.1 ± 2.2	22.6 ± 0.7
30	-2.8 ± 1.2	9.9 ± 3.5	25.7 ± 0.3
50	-0.3 ± 1.5	6.9 ± 2.1	15.7 ± 0.1
60	0.5 ± 1.4	6.5 ± 2.3	10.4 ± 1.2
150	2.5 ± 1.3	4.5 ± 1.4	8.7
320	3.7 ± 1.4	3.5 ± 2.1	9.36
350	3.5 ± 1.4	3.5 ± 2.1	8.5 ± 0.9
550	2.8 ± 1.3	3.4 ± 1.8	7.5 ± 0.1
800	3.2 ± 1.4	2.5 ± 2.0	9.7 ± 0.3
1000	7.2 ± 1.7	1.5 ± 2.5	7.9
1250	6.5 ± 1.8	6.1 ± 2.5	17.2 ± 0.2
1500	9.5 ± 2.0	0.7 ± 3.7	10.6
Spinel			
Rim	-1.2 ± 1.6	0.9 ± 1.7	2.6
Rim	-0.6 ± 1.4	2.4 ± 2.6	2.5
20	-2.6 ± 1.2	-1.3 ± 2.2	2.6
600	6.8 ± 1.5	0.4 ± 1.7	2.5
750	9.0 ± 1.2	0.6 ± 2.0	2.7
1250	6.6 ± 1.6	1.2 ± 2.5	2.5

Note :F(Mg) and $\delta^{26}\text{Mg}$ are in permil/amu and permil respectively.

*Distance from the inner boundary of the rim.

†Errors less than 0.1 are not shown.

§Data for this inclusion given in Table 4.1 are also included here.

Table 4.4: Mg-Al Data

Position* μm	F(Mg) $\pm 2\sigma_m$	$\delta^{26}\text{Mg}$ $\pm 2\sigma_m$	$^{27}\text{Al}/^{24}\text{Mg}^\ddagger$ $\pm 2\sigma_m$
E40(Type B1)\$			
Melilite Traverse			
50	4.2 ± 2.2	6.5 ± 4.2	21.0 ± 0.2
60	3.3 ± 1.3	6.7 ± 1.6	13.9 ± 0.7
80	4.8 ± 1.6	3.0 ± 2.1	14.2 ± 0.1
120	5.4 ± 2.4	0.7 ± 2.6	12.0 ± 0.2
150	4.4 ± 1.6	5.5 ± 2.5	18.9 ± 0.2
170	2.9 ± 1.3	5.9 ± 3.4	16.2 ± 0.2
230	2.4 ± 1.7	6.1 ± 3.6	18.3 ± 0.1
300	3.3 ± 1.9	4.9 ± 2.6	12.9 ± 0.1
550	3.8 ± 1.8	3.2 ± 2.8	11.4 ± 0.1
1050	0.9 ± 2.1	5.5 ± 3.4	6.8 ± 0.1
1550	0.3 ± 1.3	1.9 ± 1.7	5.8
2550	0.5 ± 1.6	3.4 ± 3.0	3.8
Spinel Traverse			
50	4.2 ± 1.6	2.4 ± 2.1	2.6
170	5.5 ± 2.1	1.1 ± 3.2	2.7
370	2.9 ± 1.6	1.2 ± 2.0	2.7
500	5.6 ± 2.0	-0.5 ± 2.7	2.6
650	4.9 ± 1.7	0.0 ± 2.8	2.6
720	3.5 ± 1.9	2.3 ± 2.6	2.6
1250	2.6 ± 1.5	1.0 ± 2.3	2.4
1300	3.3 ± 1.5	1.2 ± 2.2	2.4
1900	2.5 ± 1.9	2.9 ± 3.0	2.5
2450	1.9 ± 2.1	1.0 ± 2.7	2.5
2520	2.3 ± 1.8	2.2 ± 2.8	2.5
2555	1.9 ± 2.0	2.7 ± 3.2	2.5
2570	2.3 ± 1.7	0.1 ± 2.6	2.4
2590	3.8 ± 1.8	1.1 ± 2.7	2.7
3000	2.2 ± 1.5	3.5 ± 2.6	2.5

Note :F(Mg) and $\delta^{26}\text{Mg}$ are in permil/amu and permil respectively.

*Distance from the inner boundary of the rim.

†Errors less than 0.1 are not shown.

\$Data for this inclusion given in Table 4.1 are also included here.

Table 4.5: Mg-Al DATA

Phase	$\delta^{26}\text{Mg}^*$ $\pm 2\sigma_m$	$^{27}\text{Al}/^{24}\text{Mg}^\dagger$ $\pm 2\sigma_m$
E36(Type B2)		
Melilite 1	3.27 ± 1.97	12.38 ± 0.20
Melilite 2	1.20 ± 2.40	8.52 ± 0.10
Melilite 3	-1.61 ± 0.87	3.50 ± 0.01
Melilite 4	3.47 ± 1.60	11.28 ± 0.36
Melilite 5	2.08 ± 1.02	4.96 ± 0.28
Melilite 6	3.22 ± 1.60	6.04 ± 0.16
Melilite 7	1.55 ± 2.22	2.00 ± 0.06
Melilite 8	1.92 ± 2.00	17.33 ± 0.60
Fassaite 1	-0.92 ± 2.16	1.72 ± 0.02
E40(Type B1)		
Fassaite 1	3.0 ± 2.5	2.0
Fassaite 2	3.1 ± 1.8	1.9
Fassaite 3	0.7 ± 2.5	1.5
E44(Type B1)		
Spinel 1	-0.1 ± 1.4	2.5
Spinel 2	-0.1 ± 1.9	2.5
Spinel 3	0.4 ± 2.1	2.6
Fassaite 1	0.2 ± 4.0	2.4
Fassaite 2	1.6 ± 2.8	2.5
Fassaite 3	3.0 ± 3.6	3.4
Fassaite 4	-1.2 ± 3.5	2.6
Melilite 1	5.1 ± 2.0	9.4 ± 0.3
Melilite 2	5.4 ± 3.6	14.1
Melilite 3	3.1 ± 2.7	8.8 ± 0.2
Melilite 4	7.2 ± 3.6	11.9 ± 0.1
Melilite 5	1.5 ± 2.8	4.7
Melilite 6	1.3 ± 3.2	6.0
Melilite 7	6.1 ± 3.2	10.2 ± 0.1
Melilite 8	4.9 ± 3.4	12.7
Anorthite 1	10.9 ± 9.7	301.4 ± 33.2
Anorthite 2	25.0 ± 7.7	710.9 ± 38.4
Anorthite 3	9.8 ± 5.6	226.4 ± 12.7
Anorthite 4	8.4 ± 6.5	369.9 ± 37.9
Anorthite 5	11.6 ± 7.2	292.5 ± 46.1

Table 4.5 (Continued)

Phase	$\delta^{26}\text{Mg}^*$ $\pm 2\sigma_m$	$^{27}\text{Al}/^{24}\text{Mg}^\dagger$ $\pm 2\sigma_m$
E59(Type A)		
Melilite 1	7.38 ± 2.24	21.9 ± 0.2
Melilite 2	6.03 ± 2.40	18.1 ± 0.2
Melilite 3	3.24 ± 2.20	12.1 ± 0.2
Melilite 5	8.04 ± 4.60	23.7 ± 0.2
Melilite 6	8.44 ± 2.92	34.0 ± 0.2
E60(Type B2)		
Spinel	2.2 ± 1.5	2.5
Melilite 1	3.6 ± 2.0	0.7
Melilite 2	1.0 ± 2.4	0.7
Melilite 3	2.2 ± 1.7	1.2
Anorthite 1	10.0 ± 2.7	60.8 ± 1.1
Anorthite 2	10.6 ± 2.0	40.3 ± 1.1
Anorthite 3	44.3 ± 4.4	158.1 ± 14.5
E65(Type B1)		
Spinel 1	-2.9 ± 2.3	2.7
Spinel 2	-1.1 ± 2.8	2.4 ± 0.3
Spinel 3	-1.6 ± 2.4	2.6
Spinel 4	-0.1 ± 2.7	2.5
Spinel 5	2.5 ± 3.0	2.6 ± 0.3
Spinel 6	-0.9 ± 2.4	2.5
Spinel 7	2.3 ± 1.6	2.5
Fassaite 1	0.7 ± 3.6	1.4
Fassaite 2	-0.1 ± 4.1	2.0
Fassaite 3	0.3 ± 2.7	1.4
Melilite 1	2.7 ± 1.2	6.6
Melilite 2	2.8 ± 1.3	2.9 ± 0.3
Melilite 3	1.8 ± 2.2	3.7
Melilite 4	1.7 ± 2.9	4.8
Melilite 5	4.4 ± 1.8	13.7 ± 0.1
Anorthite 1	48.8 ± 3.4	162.3 ± 10.2
Anorthite 2	42.7 ± 4.1	136.4 ± 8.6
Anorthite 3	26.1 ± 3.1	104.4 ± 6.6

* $\delta^{26}\text{Mg}$ is in permil.

†Errors less than 0.1 are not shown.

Table 4.5 (Continued)

Phase	$\delta^{26}\text{Mg}^*$ $\pm 2\sigma_m$	$(^{27}\text{Al}/^{24}\text{Mg})$ $\pm 2\sigma_m$
GR4 (Type A)		
Melilite 1	3.4 ± 2.2	7.4 ± 0.04
Melilite 2	3.3 ± 1.8	6.1 ± 0.05
Melilite 3	7.3 ± 3.6	11.1 ± 0.15
Melilite 4	1.3 ± 3.3	8.8 ± 0.04
Melilite 5	3.4 ± 3.7	12.2 ± 0.04
Melilite 6	2.0 ± 3.4	12.1 ± 0.13
Melilite 7	-0.9 ± 2.6	5.0 ± 0.13
Melilite 8	2.0 ± 3.8	27.5 ± 0.40
Melilite 9	0.3 ± 2.9	10.9 ± 0.05
Melilite 10	3.0 ± 2.9	14.6 ± 0.60
Spinel 1	3.2 ± 2.4	2.5 ± 0.003
GR7 (Type B)		
Melilite 1	0.36 ± 1.54	1.44 ± 0.006
Melilite 2	4.32 ± 2.32	1.92 ± 0.012
Melilite 3	1.94 ± 2.08	3.55 ± 0.013
Melilite 4	3.98 ± 2.26	4.16 ± 0.033
Melilite 5	2.51 ± 3.02	3.35 ± 0.008
Melilite 6	-0.85 ± 1.99	3.21 ± 0.007
Melilite 7	1.45 ± 2.54	9.44 ± 0.398
Melilite 8	2.38 ± 1.80	5.44 ± 0.027
Melilite 9	4.51 ± 2.56	15.31 ± 0.51
Melilite 10	3.88 ± 2.14	13.76 ± 0.61
GR2 (Type C)		
Anorthite 1	12.6 ± 4.7	360.1 ± 30.1
Anorthite 2	8.3 ± 2.4	354.8 ± 11.0
Anorthite 3	6.7 ± 5.1	317.1 ± 2.6
Anorthite 4	8.4 ± 4.7	321.5 ± 3.5
Anorthite 5	8.8 ± 5.1	647.4 ± 64.1
Anorthite 6	7.6 ± 0.7	318.7 ± 2.08
Fassaite 1	0.1 ± 2.3	2.0 ± 0.003
Fassaite 2	0.6 ± 2.1	0.8 ± 0.001
Fassaite 3	0.1 ± 2.3	0.7 ± 0.001
Fassaite 4	1.0 ± 2.8	2.1 ± 0.004
Fassaite 5	2.2 ± 3.0	7.2 ± 0.004
Fassaite 6	0.4 ± 1.7	2.0 ± 0.002

$\delta^{26}\text{Mg}$ is in permil

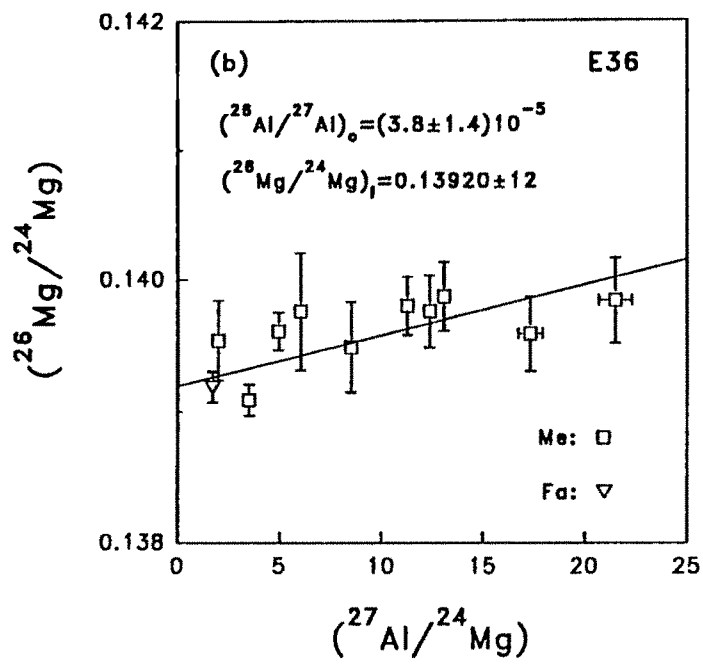
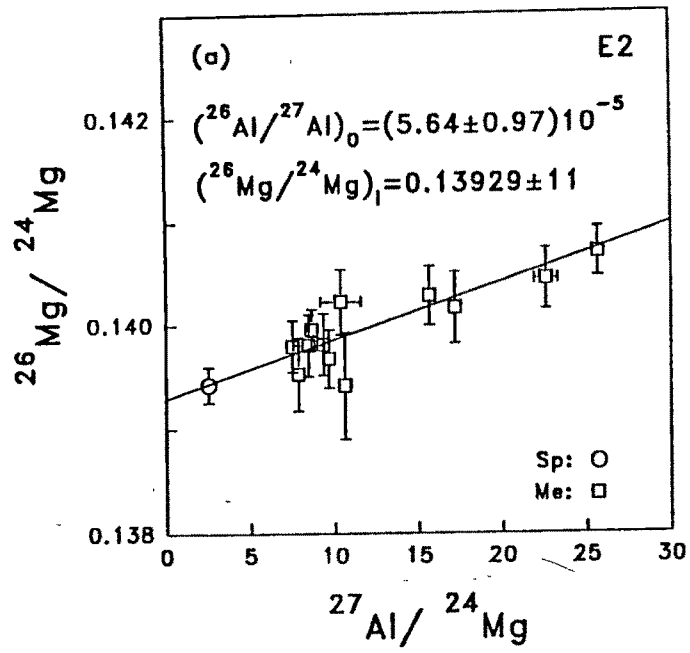


Fig.4.1

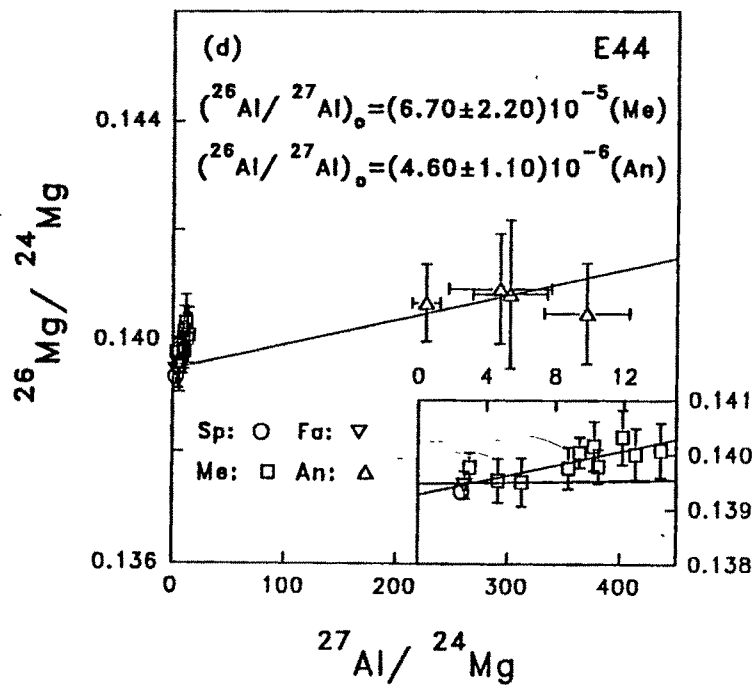
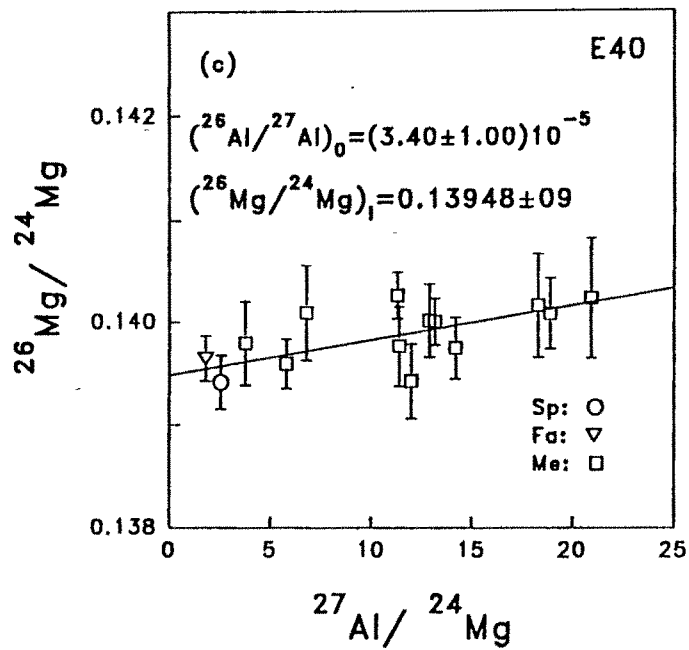


Fig.4.1 (Continued)

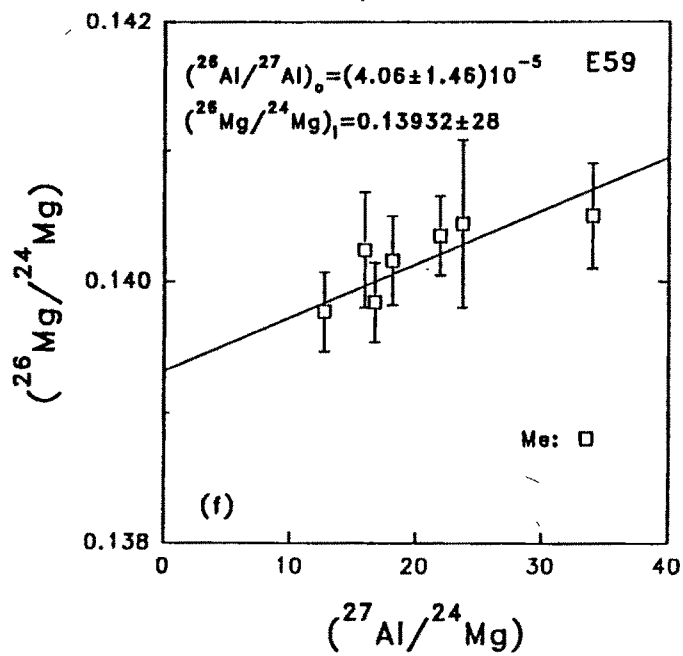
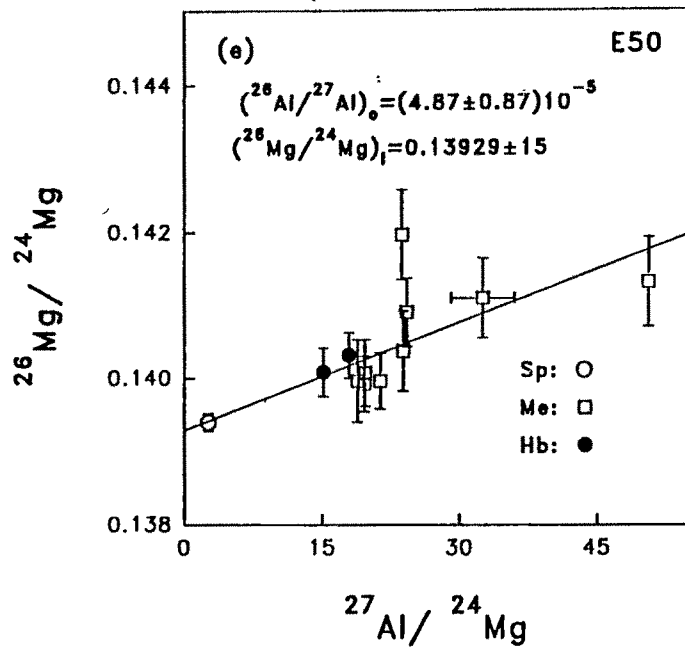


Fig.4.1 (Continued)

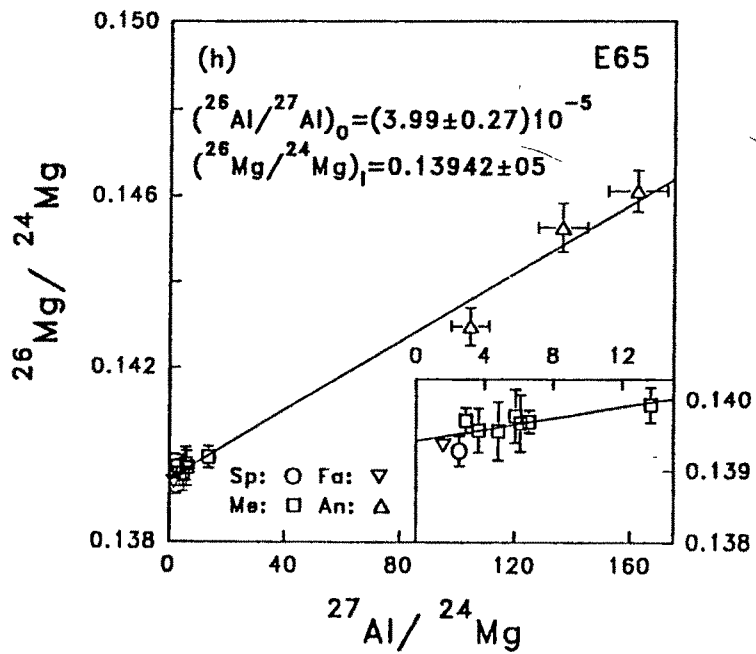
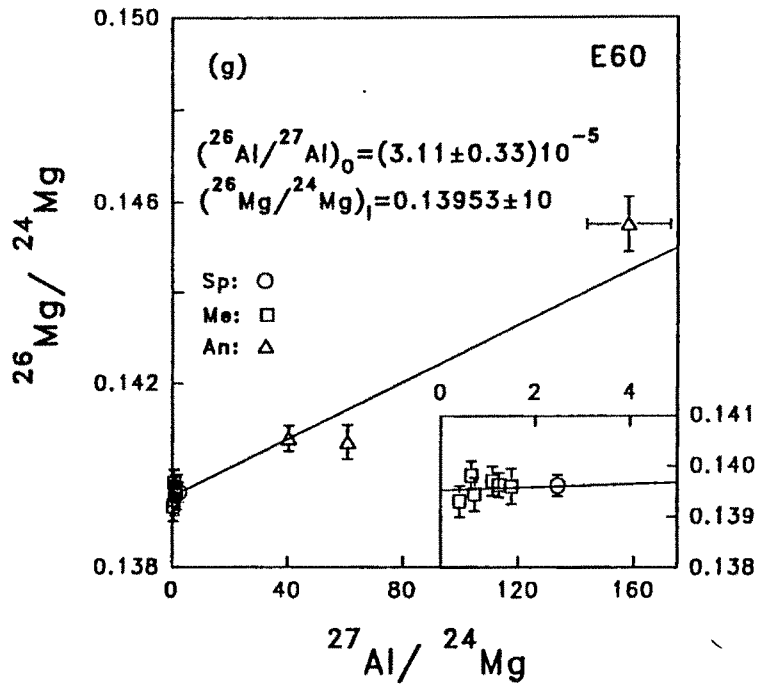


Fig.4.1 (Continued)

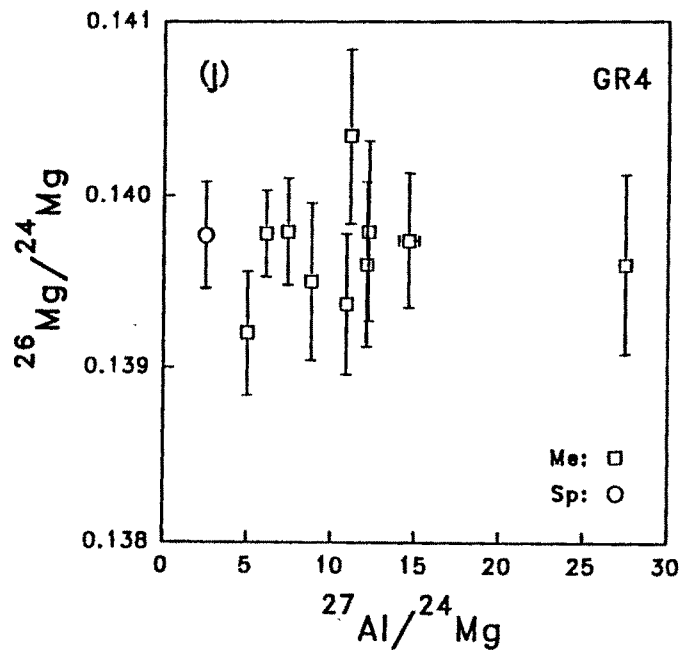
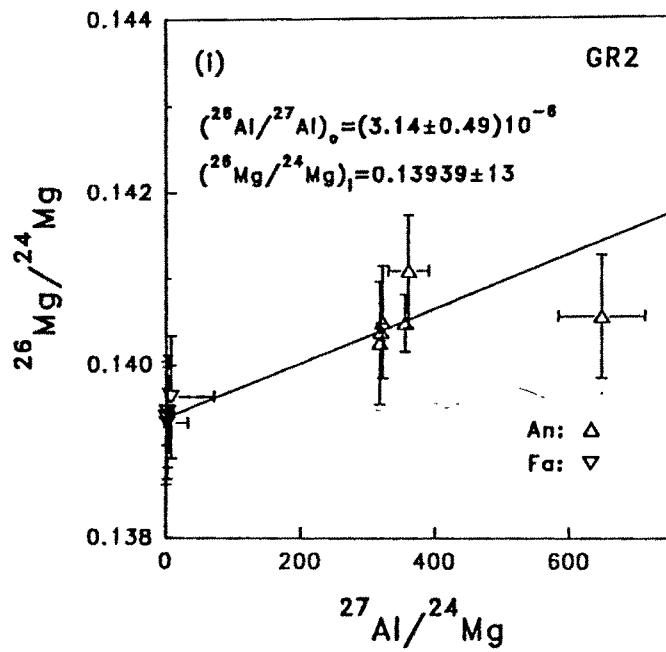


Fig.4.1 (Continued)

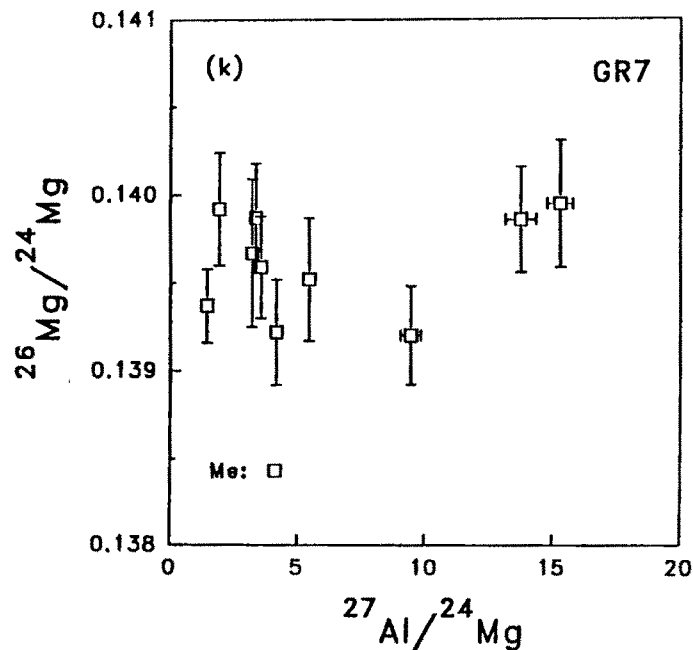


Figure 4.1: Mg-Al evolution diagram for the Efremovka CAIs E2 (type A), E36 (type B2), E40 (type B1), E44 (type B1), E50 (hibonite-rich), E59 (type A), E60 (type B2), E65 (type B1) and the Grosnaja CAI GR2 (type C), are shown in figures (a) to (i) respectively. In the case of Grosnaja CAIs GR4 (type A) and GR7 (type B) only the data have been plotted in fig(j) and fig(k) respectively. The abbreviation used for the different mineral phases that have been indicated in the figures are: Sp= spinel, Me=melilite, Fa=fassaite, An=anorthite, and Hb=hibonite. The initial $^{26}\text{Mg}/^{24}\text{Mg}$ and $^{26}\text{Al}/^{27}\text{Al}$ values for individual CAIs are also given in each figure. The two isochrons for E44 are drawn through melilite and anorthite data points assuming fassaites and spinels as common members in each case. Errors are $2\sigma_m$.

4.2 Results from K-Ca Isotopic Studies

Several of the Efremovka CAIs have been analyzed for their potassium and calcium isotopic composition with a view to look for the possible presence of the short-lived radionuclide ^{41}Ca at the time of formation of the CAIs. Previous attempts in this direction (Stegmann and Specht 1983) were not successful but there was a hint in the data of Hutcheon et al. (1984) for the presence of ^{41}Ca in the early solar system. We shall discuss some of the difficulties in carrying out such studies before presenting the results.

The short-lived radionuclide ^{41}Ca ($t_{1/2} \sim 0.1\text{Ma}$) decays to ^{41}K . If ^{41}Ca was present in the early solar system and was incorporated live into the CAIs at the time of their formation then we would observe an excess in the measured $^{41}\text{K}/^{39}\text{K}$ values in them, above the reference value of 0.072, and the measured $^{41}\text{K}/^{39}\text{K}$ will have two components :

$$\begin{aligned} \left(\frac{^{41}\text{K}}{^{39}\text{K}}\right)_m &= \left(\frac{^{41}\text{K}}{^{39}\text{K}}\right)_i + \left(\frac{^{41}\text{K}^*}{^{39}\text{K}}\right) \\ &= \left(\frac{^{41}\text{K}}{^{39}\text{K}}\right)_i + \left(\frac{^{41}\text{Ca}}{^{40}\text{Ca}}\right)_i \left(\frac{^{40}\text{Ca}}{^{39}\text{K}}\right)_m \end{aligned} \quad (4.2)$$

where i represents the initial ratio, m refers to the measured ratio and * represents the radiogenic component. As in the case of Mg-Al system, and the above relation (Eq. 4.2) represents the evolution of K-Ca isotopic system in the CAI. The intercept and slope of the best-fit line represented by (Eq.4.2) gives the initial $^{41}\text{K}/^{39}\text{K}$ and $^{41}\text{Ca}/^{40}\text{Ca}$ values at the time of closure of the K-Ca isotope system in the CAI. When Ca is present it is not possible to resolve ^{40}K from ^{40}Ca interference. Thus, although potassium consists of three isotopes (39, 40 and 41) it has to be treated as a two isotope system. *Therefore unlike the case of magnesium, it is not possible to determine the fractionation corrected residual for ^{41}K (i.e. $\delta^{41}\text{K}$).* The normal K isotopic composition measured for terrestrial minerals with Ca/K ratios ranging from 10^{-3} to $\sim 3 \times 10^6$ (Tables 2.5 and 4.6) suggest that the isotopic mass fractionation in the case of potassium isotopes must be small (\leq a few permil/amu). It

may be noted that instrumental mass fractionation generally favours the lighter isotopes and as such it will tend to suppress the signal at ^{41}K relative to ^{39}K . On the other hand, since the coarse-grained CAIs are derived from evaporative residues, one may expect an enrichment of the heavy isotopes (^{41}K relative to ^{39}K). However, in general the magnitude of instrumental mass fractionation far exceed intrinsic mass fractionation and we have neglected any possible effect of isotopic mass fractionation in analyzing the K isotopic data.

The isotopic analyses were carried out by cycling the magnet through the masses ^{39}K , ^{41}K , ^{40}CaH , ^{42}Ca , [$^{43}\text{Ca} - \Delta\text{M}$; $\Delta\text{M} = (43/41)(^{40}\text{CaH} - ^{41}\text{K})$], and ^{43}Ca . Each individual analysis consisted of 10-12 blocks of 5-6 cycles each. Ions from a restricted area of the sample surface (10 μm) were accepted during isotopic analysis by limiting the size of the field aperture to avoid contributions from the neighbouring phases and possible surface contamination from outside the sputtered spot. Proper care was taken during sample preparation to remove any K deposited on the sample surface while polishing. This was achieved by slowly heating the epoxy mounted samples in ultra-pure water (filtered through MilliporeTM Milli-Q Plus system) for a period of one to two hours. A pre-burn of the sample surface was conducted for ~ 30 minutes so that Ca/K reaches a steady value. Hibonite, perovskite and pyroxene with high Ca and low K content are ideally suited for K isotopic studies, while melilite and anorthite have Ca/K values $< 10^5$ and are found to be unsuitable for such studies.

Perovskites in E50, and pyroxenes in E65 and E44 were analyzed for their potassium and calcium isotopic composition. E50 and E65 have well behaved Mg-Al systematics with initial $^{26}\text{Al}/^{27}\text{Al}$ close to the canonical value of 5×10^{-5} . Even though the disturbed Mg-Al isotopic systematics in E44 suggest Mg exchange between melilite and anorthite in this CAI, the pyroxenes appear to be undisturbed with no petrographic evidence of secondary alteration. The results obtained in the present study are given in Table 4.6. The $^{40}\text{Ca}/^{39}\text{K}$ values were computed by using the measured ion ratios and the relative yield factor of 3.2 (Table 2.4, Chapter 2) favouring K. The perovskite grains from E50 have lower Ca/K values compared to the terrestrial perovskite. This is probably because of contribution

from neighbouring melilite. Analyses of hibonite grains from E50 were not attempted for similar reasons. The $^{41}\text{K}/^{39}\text{K}$ values (Table 4.6) have been corrected for contribution to the ^{41}K signal from i) unresolvable ($^{40}\text{Ca}^{42}\text{Ca}$)⁺⁺ interference, and ii) contribution from the tail of the ^{40}CaH peak (see section 2.3.3, Chapter2). The typical signal at mass ^{41}K ranges from 0.3-0.8(c/s). The hydride contribution estimated from the count rate at ($^{43}\text{Ca} - \Delta\text{M}$) was found to be very small and in general it was less than the counting system background. The ($^{40}\text{Ca}^{42}\text{Ca}$)⁺⁺ correction is proportional to the measured ($^{40}\text{Ca}^+ / ^{39}\text{K}^+$) value in the sample and the magnitude of this correction ranges from a few percent to $\sim 70\%$ of the measured ($^{41}\text{K}^+ / ^{39}\text{K}^+$) values.

It can be seen from Fig.5.7 that the meteoritic phases with high Ca/K ($\geq 3 \times 10^5$) show clear evidence of excess ^{41}K ; with the measured $^{41}\text{K}/^{39}\text{K}$ values much above the reference value of 0.072. The large errors in the $^{41}\text{K}/^{39}\text{K}$ ratios are due to poor counting statistics at mass 41 and sometimes at mass 39 which are typically of the order of $\leq 4\%$ (at 1σ level), and the error associated with doubly charged calcium interference (see Table 4.6 footnote). The excess signal at mass 41, after all the corrections, ranges from 0.05 to 0.12(c/s), which is much above the dynamic background of the counting system, ≤ 0.01 (c/s). This excess accounts for ~ 10 -25% of the measured count rates at this mass. The slope of the best fit correlation line between $^{41}\text{K}/^{39}\text{K}$ and $^{40}\text{Ca}/^{39}\text{K}$ is $(1.6 \pm 0.3) \times 10^{-8}$ which represents the value of initial ($^{41}\text{Ca}/^{40}\text{Ca}$) at the time of formation of Efremovka CAIs. The intercept has a value (0.07134 ± 0.00085) which is close to the reference value of 0.072. We shall consider the plausible causes for excess ^{41}K in Efremovka CAIs and its implications towards early solar system processes in the next chapter.

Table 4.6: K-Ca Data

Sample	$^{40}\text{Ca}/^{39}\text{K}^{\dagger}$ $\pm 2\sigma_m$	$^{41}\text{K}/^{39}\text{K}^{\dagger}$ $\pm 2\sigma_m$
Terrestrial Minerals		
Microcline*	$\sim 10^{-3}$	0.07187 ± 0.0001
Anorthositic Glass ** (An-Mg-5)	8.6×10^3	0.07107 ± 0.0013
Pyroxene 1** (Ti-PX-1)	2.1×10^4	0.07301 ± 0.0012
Pyroxene 2** (CAI-PX-1)	3×10^6	0.06999 ± 0.0064
Perovskite [®]	$\sim 4 \times 10^6$	0.06475 ± 0.0091
Efremovka CAIs		
E50		
Perovskite 1	$(1.69 \pm 0.01) \times 10^5$	0.07476 ± 0.0022
Perovskite 2	$(5.95 \pm 0.01) \times 10^4$	0.06992 ± 0.0020
Perovskite 3	$(1.36 \pm 0.01) \times 10^5$	0.07365 ± 0.0020
E65		
Pyroxene 1	$(7.30 \pm 0.81) \times 10^4$	0.07399 ± 0.0017
Pyroxene 2	$(2.67 \pm 0.29) \times 10^5$	0.07782 ± 0.0044
Pyroxene 3	$(5.87 \pm 0.85) \times 10^4$	0.07176 ± 0.0018
Pyroxene 4	$(9.73 \pm 1.33) \times 10^4$	0.07122 ± 0.0020
Pyroxene 5	$(1.75 \pm 0.28) \times 10^5$	0.07441 ± 0.0028
Pyroxene 6	$(1.52 \pm 0.42) \times 10^5$	0.07646 ± 0.0039
Pyroxene 7	$(9.34 \pm 0.54) \times 10^5$	0.08390 ± 0.0085
Pyroxene 8	$(9.87 \pm 0.95) \times 10^5$	0.09311 ± 0.0107
Pyroxene 9	$(5.94 \pm 0.66) \times 10^5$	0.08303 ± 0.0088
Pyroxene 10	$(1.28 \pm 0.06) \times 10^6$	0.09738 ± 0.0100
Pyroxene 11	$(3.55 \pm 0.30) \times 10^6$	0.08934 ± 0.0426
Pyroxene 12	$(2.18 \pm 0.11) \times 10^6$	0.09851 ± 0.0218
Pyroxene 13	$(1.15 \pm 0.07) \times 10^6$	0.08862 ± 0.0131
Pyroxene 14	$(1.05 \pm 0.08) \times 10^6$	0.08874 ± 0.0081
Pyroxene 15	$(8.92 \pm 0.62) \times 10^6$	0.13293 ± 0.0628
Pyroxene 16	$(2.68 \pm 0.39) \times 10^7$	0.48472 ± 0.3050
E44		
Pyroxene 1	$(2.84 \pm 0.39) \times 10^6$	0.15437 ± 0.0398
Pyroxene 2	$(2.44 \pm 0.14) \times 10^6$	0.13015 ± 0.0103

Table 4.6(Continued)

* US National Museum Standard (USNM 143966).

**Samples prepared at Caltech (Courtesy I. Hutcheon).

@Sample obtained from Vernadsky Institute, Moscow.

†The ($^{40}\text{Ca}/^{39}\text{K}$) values for *terrestrial perovskite and meteoritic phases* were obtained from ion microprobe data using an ion yield of 3.2, favouring K over Ca during sputtering. The yield factor is based on terrestrial pyroxene with high Ca/K.

‡Values are corrected for ($^{40}\text{Ca}^{42}\text{Ca}$)⁺⁺ interference. The value for [$^{40}\text{Ca}^{43}\text{Ca}$]⁺⁺/ $^{43}\text{Ca}^+$ ratio for pyroxene and perovskite are $(2.64 \pm 0.09) \times 10^{-5}$ and $(2.79 \pm 0.04) \times 10^{-5}$ respectively. The magnitude of ($^{40}\text{Ca}^{42}\text{Ca}$)⁺⁺ correction is given by:

$$[\text{}^{40}\text{Ca}^{43}\text{Ca}]^{++}/^{43}\text{Ca}^+ \times (^{42}\text{Ca}^+ / ^{40}\text{Ca}^+) \times (^{40}\text{Ca}^+ / ^{39}\text{K}^+)$$

where ($^{40}\text{Ca}^+ / ^{42}\text{Ca}^+$) = 151.02